

When does vapor pressure deficit drive or reduce evapotranspiration?

A. Massmann¹, P. Gentine¹, C. Lin²

⁴¹Department of Earth and Environmental Engineering, Columbia University, New York, NY 10027

⁵²Department of Hydraulic Engineering, Tsinghua University, Beijing, CN

Key Points:

- ⁷ • = enter point 1 here =
- ⁸ • = enter point 2 here =
- ⁹ • = enter point 3 here =

10 **Abstract**

11 = enter abstract here =

12 **1 Introduction**

13 Changes to vapor pressure deficit (VPD) alter the atmospheric demand for water from
 14 the land surface. Traditionally, atmospheric scientists and hydrometeorologists generally
 15 think that an increase in atmospheric demand induces an increases in evapotranspiration
 16 (ET) (citations?). This possible misconception developed in part due to the proliferation of
 17 studies examining potential ET rather than estimates of ET itself (citations?). In contrast, plant
 18 physiologists know that stomata have evolved to optimally regulate the exchange of water
 19 and carbon, and tend to close in response to increased atmospheric dryness [??*MEDLYN*
 20 *et al.*, 2011]. Therefore, an increase (decrease) in VPD may not correspond to an increase
 21 (decrease) in ET because stomatal closure (opening) can cancel the effects of shifts to atmo-
 22 spheric demand.

← This section
needs to be
fleshed out,
and I defi-
nitely need
to add more
citations

23 Quantifying the plant response to a perturbation to atmospheric VPD increases our un-
 24 derstanding of land surface response to shifts in atmospheric conditions. If plant response
 25 reduces ET in response to atmospheric drying then soil moisture will be conserved. An in-
 26 crease in ET in reponse to atmospheric drying will reduce soil moisture, but contribute in-
 27 creased moisenting to the atmosperhere. Clearly, the sign and magnitude of land-surface
 28 responsedrives the co-evolution of the atmosphere and land-surface at many timescales, from
 29 diurna to interdecadal.

30 In order to quantify plant response to perturbations to atmospheric demand for water,
 31 we apply a Penman-Monteith framework to eddy-covariance observation spanning various
 32 biomes and climates. Section 2 describes the data used, Section 3 derives the framework,
 33 Section 4 presents results, and Section 5 discusses conclusions. The goal of this paper is
 34 to use reasonable approximations as a tool to increase intuition for plant response to atmo-
 35 spheric drying. This intuition will aid interpretation of observations and full complexity cli-
 36 mate models.

37 **2 Methods**

38 The Penman-Monteith equation (hereafter PM) estimates ET as a function of atmo-
 39 spheric and land-surface variables:

$$40 \quad ET = \frac{\Delta R + g_a \rho_a c_p D_s}{\Delta + \gamma(1 + \frac{g_a}{g_s})}, \quad (1)$$

41 where variable definitions are given in Table 1. *MEDLYN et al.* [2011] developed a
 42 model for g_s by combining optimal photosynthesis theory with empirical approaches. The
 43 result for leaf-scale stomatal resistance was:

$$44 \quad g_{l-s} = g_0 + 1.6 \left(1 + \frac{g_1}{\sqrt{D_s}} \right) \frac{A}{c_s} \quad (2)$$

45 This can be adapted to an ecosystem-scale stomatal resistance by multiplying by leaf
 46 area index (LAI) and converting units to m s^{-1} :

$$47 \quad g_s = \text{LAI} \frac{RT}{P} \left(g_0 + 1.6 \left(1 + \frac{g_1}{\sqrt{D_s}} \right) \frac{A}{c_s} \right) \quad (3)$$

48 While Equation 3 can be used in PM, it will make analytical work with the function
 49 intractable because A is a function of ET itself. To remove dependence of ET on A we can
 50 use the semi-empirical results of *Zhou et al.* [2015]. *Zhou et al.* [2015] showed that:

$$51 \quad uWUE = \frac{GPP \cdot \sqrt{D}}{ET} \quad (4)$$

52 is relatively constant across time and space (within plant functional type). If, following *Lin*
 53 *et al.* [2015], we approximate g_0 as 0, we can use $uWUE$ to remove A from g_s in a way that
 54 makes PM analytically tractable:

$$55 \quad g_s = \frac{\text{LAI}}{\text{LAI}_{ref}} \frac{RT}{P} 1.6 \left(1 + \frac{g_1}{\sqrt{D_s}} \right) \frac{uWUE \cdot ET}{c_s \sqrt{D}} \quad (5)$$

56 Note that $uWUE$ is fit on the ecosystem scale in *Zhou et al.* [2015] so it already has an
 57 implicit LAI_{ref} reflective of the average LAI in *Zhou et al.* [2015]'s fits. So the LAI term
 58 in Equation 2 becomes a term we call $\frac{\text{LAI}}{\text{LAI}_{ref}}$, which is a measure of how close the observed
 59 LAI is to the LAI_{ref} in *Zhou et al.* [2015].

60 Next, plugging Equation 5 into Equation 1 and rearranging gives:

$$61 \quad ET = \frac{\Delta R + \frac{g_a P}{T} \left(\frac{c_p D_s}{R_{air}} - \frac{\text{LAI}_{ref}}{\text{LAI}} \frac{\gamma c_s \sqrt{D}}{R * 1.6 uWUE (1 + \frac{g_1}{\sqrt{D}})} \right)}{\Delta + \gamma} \quad (6)$$

62 We can then take the derivative with respect to D to analytically determine ecosystem
 63 response to atmospheric demand perturbations:

$$64 \quad \frac{\partial ET}{\partial D} = \frac{g_a P}{T(\Delta + \gamma)} \left(\frac{c_p}{R_{air}} - \frac{\text{LAI}_{ref}}{\text{LAI}} \frac{\gamma c_s}{1.6 R * \text{uWUE}} \left(\frac{2g_1 + \sqrt{D}}{2(g_1 + \sqrt{D})^2} \right) \right) \quad (7)$$

65 Note that given yearly uWUE from *Zhou et al.* [2015], g_1 from *Lin et al.* [2015] [as presented
 66 in *Franks et al.*, 2017], and observations of R, T, P, D_s , and wind speed (WS), the only un-
 67 known is $\frac{\text{LAI}}{\text{LAI}_{ref}}$. With flux tower observations of ET, $\frac{\text{LAI}}{\text{LAI}_{ref}}$ will then be uniquely deter-
 68 mined for each observation through Equation 6:

$$69 \quad \frac{\text{LAI}}{\text{LAI}_{ref}} = - \frac{g_a \gamma c_s \sqrt{D_s} P}{(ET(\Delta + \gamma) - \Delta R - g_a \rho_a c_p D_s) 1.6 R T \text{ uWUE} (1 + \frac{g_1}{\sqrt{D_s}})} \quad (8)$$

70 This $\frac{\text{LAI}}{\text{LAI}_{ref}}$ is some part a “true” deviation of LAI from LAI_{ref} in *Zhou et al.* [2015],
 71 and some part model and observational error, including assumptions about constant g_1 and
 72 $uWUE$. By calculating a unique $\frac{\text{LAI}}{\text{LAI}_{ref}}$ for each observation we will propagate any model
 73 and observational uncertainty forward into our expression for $\frac{\partial ET}{\partial D}$.

75 3 Data

76 We use data from FLUXNET2015. Because g_1 coefficients [*Lin et al.*, 2015] and uWUE
 77 were only both available for five plant functional types (PFTs - see Table 2), only 56 of the 77
 78 sites were used. Figure 1 presents each site and its plant functional type.

84 We restrict our analysis to the daytime (sensible heat $> 5 \text{ W m}^{-2}$ and shortwave radia-
 85 tion $> 50 \text{ W m}^{-2}$) when there is no precipitation and the plants are growing (GPP $> 10\%$ of
 86 the 95th percentile). Also, because some sites use half hourly data but some use hourly, we
 87 aggregate all data to hourly averages. Only times with good quality control flags are used.

← map needs
to be im-
proved - it's
a placeholder
for now

88 4 Results

89 By construction, the variability in the LAI term (Equation 8) contains all model and
 90 observational uncertainties. LAI also has physical meaning corresponding to “true” leaf area,
 91 and we expect that it would be approximately $O(1)$, especially because uWUE is fit in *Zhou*
et al. [2015] at the ecosystem-level. We can have some confidence in our framework, in-
 92 cluding the assumption of constant uWUE, if calculated LAIs are generally $O(1)$. Figure 2
 93 presents the histogram of calculated LAIs with outliers (lowest and highest 5% percent) and

← This GPP
thresholding
was used by
Changjie, do
you know if
there is a ci-
tation for it?
Otherwise it
seems like
something a
reviewer
would have
issue with as
it is arbitray

74

Table 1. Definition of symbols and variables

Variable	Description	Units
e_s	saturation vapor pressure	Pa
T	temperature	K
Δ	$\frac{\partial e_s}{\partial T}$	Pa K ⁻¹
R	net radiation at land surface minus ground heat flux	W m ⁻²
g_a	atmospheric conductance	m s ⁻¹
ρ_a	air density	kg m ⁻³
c_p	specific heat capacity of air at constant pressure	J K ⁻¹ kg ⁻¹
D	VPD	Pa
γ	psychrometric constant	Pa K ⁻¹
g_s	stomatal conductance	m s ⁻¹
g_{l-s}	leaf-scale stomatal conductance	mol m ⁻² s ⁻¹
R^*	universal gas constant	J mol ⁻¹ K ⁻¹
LAI	leaf area index	-
$\frac{LAI}{LAI_{ref}}$	ratio of LAI to LAI _{ref} in Zhou <i>et al.</i> [2015]	-
c_s	CO ₂ concentration	μ mol CO ₂ mol ⁻¹ air

^aFootnote text here.

79

80

81

Table 2. Plant functional types, their abbreviation, Medlyn coefficient [from Lin *et al.*, 2015], and uWfUE [from Zhou *et al.*, 2015]. Note that units are converted such that the quantities fit into Equations 1-8 with the variables in Table 1.

Abbreviation	PFT	g_1 (Pa ^{0.5})	uWUE (μ -mol [C] Pa ^{0.5} J ⁻¹ [ET])
CRO	cropland	183.1	3.80
CSH	closed shrub	148.6	2.18
DBF	deciduous broadleaf forest	140.7	3.12
ENF	evergreen needleleaf forest	74.3	3.30
GRA	grassland (C3)	166.0	2.68

^aFootnote text here.

95 nonphysical values ($LAI < 0.$) removed. All remaining LAI values are $O(1)$ which provides
96 confidence in model framework.

100 An additional concern is that the LAI term may in fact be some function of D , in which
101 case the dependence would need to be accounted for when taking the derivative. Figure 3.
102 plots the joint distribution of LAI and VPD, and shows that LAI is very weakly a function of
103 VPD. Given this weak dependence, we argue that Equation 7 is a valid approximation for ET
104 response to D .

← Figs 2 and 3
can probably
be combined
- the his-
togram of
LAI is shown
in Fig 3

109 Before diving into calculated values of $\frac{\partial ET}{\partial D}$, it is useful to consider the functional
110 form of Equation 7. There are three terms: a scaling term for the full expression we will call
111 Term 1 ($\frac{g_a P}{T(\Delta+\gamma)}$), a relatively constant offset we will call Term 2 ($\frac{c_p}{R_{air}}$), and a variable term
112 we will call Term 3 ($\frac{\gamma c_s}{LAI 1.6 R \text{ uWUE}} \left(\frac{2g_1 + \sqrt{D}}{2(g_1 + \sqrt{D})^2} \right)$). All variables are positive, so the relative
113 magnitude between Term 2 and Term 3 will determine the sign of the derivative, while Term
114 1 will scale the expression larger or smaller.

115 In Term 1, $\frac{P}{T} \propto \rho$, so this should vary little relative to g_a and Δ . γ should also be rel-
116 atively constant. So the scaling term, Term 1, should be primarily a function of g_a and tem-
117 perature (through the function Δ). While temperature range may vary for PFT, the functional
118 form of Δ will be the same. g_a will vary strongly with PFT due to the importance of surface
119 roughness. However, the coefficient of variability for both g_a and Term 1 is relatively con-
120 stant across PFT, suggesting that the influence of g_a on the relative (to the mean) variability
121 of Term 1 is approximately similar across PFT.

122 Figure 4A shows Term 1 normalized by mean g_a (calculated for each plant functional
123 type), and confirms that much of the relative variability of Term 1 is contained in the g_a
124 term's relative variability. Generally, T has less of a role. Additionally, the impact of T on
125 the relative variability increases with increasing g_a .

126 While the relative variability of Term 1 is similar across PFT, the absolute value of
127 Term 1 varies strongly across PFT. Figure 4B shows Term 1 evaluated with the mean g_a for
128 each PFT, and at the range of observed temperatures for each PFT. As expected, for the tree
129 PFTs (DBF, ENF) Term 1 is much larger and the temperature dependence is much stronger.
130 Systematic differences in observed temperatures also cause differences in the average mag-
131 nitude of Term 1. For example, ENF experiences on average colder temperatures and is thus
132 more likely to have a larger scaling term. Additionally, because $\text{std}(g_a) \propto \overline{g_a}$, the spread of

133 Term 1 due to g_a variability will be larger for the tree PFTs, although this is not shown for
 134 simplicity. To summarize, the variability of Term 1 within each PFT will look like Figure 4A
 135 for each PFT, but the scale of the x and y-axis will increase or decrease according to mean g_a
 136 observed in Figure 4B.

141 Term 2 minus Term 3 determines the sign and magnitude that the scaling Term 1 is
 142 multiplied by. If we assume that c_s variability is relatively less than LAI and D variability,
 143 then variability within PFT will be solely determined by LAI and D . Figure 5 shows how
 144 (Term 2 - Term 3) varies with D and LAI, as a function of PFT. In Figure 5a lower uWUE
 145 and LAI shift the distribution of (Term 2 - Term 3) towards negative values. Additionally, the
 146 smaller g_1 , the greater the relative D dependence of (Term 2 - Term 3). This is observed
 147 most strongly for the ENF PFT, which has the smallest g_1 (74.31).

154 Figure 5b shows the location of the minima of ET, as a function of LAI and D . For any
 155 LAI or VPD less (more) than these curves, Term 2 - Term 3 will be negative (positive). It is
 156 clear that the portion of VPD observations below/above these curves will be a strong func-
 157 tion of LAI. However, we can see some general trends. For CSH, $\frac{\partial ET}{\partial D}$ should be negative
 158 for the vast majority of observed LAI and VPD. The split appears to be more even among
 159 ENF, GRA, and DBF, and we might expect a greater frequency of positive $\frac{\partial ET}{\partial D}$ for CRO.

160 Table 3 confirms these expectations for PFT behavior of $\frac{\partial ET}{\partial D}$. For all PFTs except
 161 for CRO, average $\frac{\partial ET}{\partial D}$ is less than zero. However, $\frac{\partial ET}{\partial D}$ evaluated at the average of all vari-
 162 ables (e.g. LAI, T , c_s , D) is only negative for CSH and GRA. And, DBF in addition to CRO
 163 experiences $\frac{\partial ET}{\partial D} < 0$ less than half the time. These observations highlight the effect of the
 164 nonlinear function in Figure 5: $\frac{\partial ET}{\partial D}$ has a much steeper slope when the function is negative,
 165 and is thus more likely to be large magnitude.

166 The units of $\frac{\partial ET}{\partial D}$ make it difficult to interpret if D is even a meaningful contributor to
 167 ET's variability. To understand D 's contribution better, we use a linear approximation and
 168 present $\frac{\partial ET}{\partial D}$ multiplied by D 's standard deviation. The D 's contribution to ET's variabil-
 169 ity ranges between 16 - 20 W m⁻² for all PFTs except for CSH, which is about 51 W m⁻².
 170 Another meaningful comparison is to $\frac{\partial ET}{\partial R} * std(R)$, as net radiation generally the driver of
 171 ET (cite joe berry here). For all PFTs except for CSH D contributes between 14.5 - 20.5 %
 172 of R 's contribution to variability. For CSH the portion is much larger, about 44 %. However
 173 it is important to note that a linear approximation about a mean base state is probably not a
 174 very good approximation across the range of variability, so these values are just estimates of

190

Table 3. Statistics of $\frac{\partial ET}{\partial D}$ as a function of PFT.

PFT	$\frac{\partial ET}{\partial VPD}$	$\overline{\frac{\partial ET}{\partial D}}(T, \dots, D)$	$\overline{\frac{\partial ET}{\partial D}}(T, \dots, D) * \text{std}(D)$	$\frac{\overline{\frac{\partial ET}{\partial D}}(T, \dots, D) * \text{std}(D)}{\overline{\frac{\partial ET}{\partial R}}(T, \dots, D) * \text{std}(R)}$	fraction $\frac{\partial ET}{\partial VPD} < 0$
CRO	0.000853	0.026241	18.523659	0.203022	0.473311
CSH	-0.108234	-0.091526	50.861613	0.439379	0.931660
DBF	-0.012727	0.013794	19.734435	0.164241	0.461674
ENF	-0.034087	0.000706	16.611852	0.148548	0.534425
GRA	-0.019637	-0.000921	16.798083	0.173552	0.631735

^aFootnote text here.

175

D's contribution to ET's variability. Regardless, *D*'s variability is certiantly a non-negligable contributor to *ET*'s variability.

177

So far, idealized plots and statistics have illuminated the form of $\frac{\partial ET}{\partial D}$ and how it varies with PFT. Large mean LAI and uWUE shifts CRO and DBF towards positive $\frac{\partial ET}{\partial D}$. However, the strongly nonlinear function of $\frac{\partial ET}{\partial D}$ at $\frac{\partial ET}{\partial D} < 0$ pushes $\overline{\frac{\partial ET}{\partial D}}$ negative for DBF (it does not do this for CRO because of CRO's high g_1). ENF's low g_1 value increases the dependence of $\frac{\partial ET}{\partial D}$ on *D*, and makes the function more strongly nonlinear. This has the side effect of pushing $\overline{\frac{\partial ET}{\partial D}}$ negative further than other PFTs for a given fraction $\frac{\partial ET}{\partial D} < 0$ and magnitude $\overline{\frac{\partial ET}{\partial D}}(T, \dots, D)$. GRA shows the opposite behavior; a relatively high g_1 makes the function more linear, decreasing the magnitude of $-\overline{\frac{\partial ET}{\partial D}}$ for a given [large] fraction $\frac{\partial ET}{\partial D} < 0$ and negative $\overline{\frac{\partial ET}{\partial D}}(T, \dots, D)$ (although g_a and Term 1 also probably have a role in this). Finally, low uWUE of CSH pushes to toward by far the lowest values $\frac{\partial ET}{\partial D}$ (Figure 5). Variability in *D* accounts for the largest about of *ET* variability for CSH. For the other PFTs, *D* contributes less to *ET* variability, but still represents about 15-20 % of *R*'s contributions to ET variability.

178

179

180

181

182

183

184

185

186

187

188

189

190

191

4.1 Full observations of $\frac{\partial ET}{\partial D}$

192

Now that we have an intuitive understanding of $\frac{\partial ET}{\partial D}$'s behavior, we are equipped to interpret fully realistic plots of $\frac{\partial ET}{\partial D}$ for each PFT. Figure 6 presents calculated $\frac{\partial ET}{\partial D}$ where, unless otherwise noted, all variables in Equation 7 are allowed to vary. Each column is a different quantity related to $\frac{\partial ET}{\partial D}$, and each row is a different PFT.

196 The full observations generally confirm expectations from Section 4. CRO has the
 197 most positive values of $\frac{\partial ET}{\partial D}$, $\frac{\partial ET}{\partial D}$ is almost always negative for CSH, and response depends
 198 more with the environmental conditions for the other PFTs (especially ENF). Through the
 199 columns of Figure 6 we can see the impact of LAI and g_a on the variability of $\frac{\partial ET}{\partial D}$. g_a 's
 200 scaling (included in columns 1 and 3) alters the magnitude considerably. *LAI* variability
 201 (included in columns 1 and 2) adds a lot of additional noise to the signal of $\frac{\partial ET}{\partial D}$, which is
 202 slightly undesirable given LAI's role in representing model and observational uncertainty.
 203 However, the general story with the noise appears to match the cleaner signal when *LAI* is
 204 help constant and D_{ETmin} is clearly visible . One exception is possibly with GRA, for which
 205 uncertainty represented in LAI is high and causes the full complexity plots (Columns 1 and
 206 2) to not match well with LAI held fixed (Columns 3 and 4).

← I really need
to make
these plots
better - way
too much
overlapping
of points
that hurts the
story

207 For ENF and GRA D_{ETmin} does not appear to be only a function of LAI (most observ-
 208 able in Column 4). It turns out that the site to site variability in γ causes D_{ETmin} to vary,
 209 which is not discussed in the previous section. The impact is observable in both ENF and
 210 GRA, but especially for ENF which has a larger $\frac{\partial^2 ET}{\partial^2 D}$ than the other PFTs.

211 In general the full complexity plots of $\frac{\partial ET}{\partial D}$ match our expectations, even with the large
 212 sensitivity to LAI measures of uncertainty observed in Figure 5. Our LAI-based method of
 213 uncertainty propagation blurs the idealized expectations the most for GRA, and also has a
 214 considerable effect for CRO. We therefor have the most confidence in our conclusion based
 215 on Equation 7 for PFTS CSH, DBF, and ENF, as the full complexity plots with uncertainty
 216 included closely match the story when LAI is held fixed. **see somewhat preferred alternate
 217 figure 7 .

← I think I like
the alternate
plot much
more as
thinking in
terms of T
and RH is
easier, and
it makes the
story easier
to see at rel-
atively low
temperatures.
However,
I used the
other plot be-
cause Fig 5
does not dis-
cuss things
in terms of
temperature,
as this would
make things
more compli-
cated (adding
another di-
mension).
I could just
include both
versions
of figure 6

226 5 Conclusions

227 The idealized representation of ET used here is successful in developing intuition for
 228 how ET responds to changes in D . This intuition will aid the community in interpreting ob-
 229 servations and output from sophisticated full complexity climate models.

230 The idealized framework leads to the following general conclusions:

- 231 • Aerodynamic resistance plays an important role of scaling $\frac{\partial ET}{\partial D}$. This is a leading
 232 order effect for observing higher magnitude responses in DBF and ENF.

- In general, CSH has the most negative (i.e. ET reduced) response to increases in D (atmospheric drying). So CSH plants will almost always try and conserve water, effectively reducing ET with dry atmospheric perturbation.
- Additionally for CSH, D variability contributes the most to ET variability.
- CRO has the most positive response (i.e. ET increased) in response to increases in D . This is consistent with CROs that may be evolved or bred to thrive in non-water-limited environments.
- The response is more a function of the environment for DBF, ENF, and GRA. Because as VPD increases the response is more likely to be positive, if RH is fixed then the response will be more likely to be positive at warmer T, or if T is fixed the response is more likely to be positive with decreasing RH.
- ENF has the strongest dependence on environmental conditions due to its small g_1 .
- Model and observational uncertainty is highest for GRA and CRO, so conclusions about those PFTs should be tempered.
- However, inclusion of uncertainty doesn't alter conclusions about DBF, ENF, and CSH.

The intuition developed using this framework can be used to understand how the land surface will respond and contribute to changes in the environment.

Acknowledgments

This work used eddy covariance data acquired and shared by the FLUXNET community, including these networks: AmeriFlux, AfriFlux, AsiaFlux, CarboAfrica, CarboEuropeIP, CarboItaly, CarboMont, ChinaFlux, Fluxnet-Canada, GreenGrass, ICOS, KoFlux, LBA, NECC, OzFlux-TERN, TCOS-Siberia, and USCCC. The ERA-Interim reanalysis data are provided by ECMWF and processed by LSCE. The FLUXNET eddy covariance data processing and harmonization was carried out by the European Fluxes Database Cluster, AmeriFlux Management Project, and Fluxdata project of FLUXNET, with the support of CDIAC and ICOS Ecosystem Thematic Center, and the OzFlux, ChinaFlux and AsiaFlux offices.

References

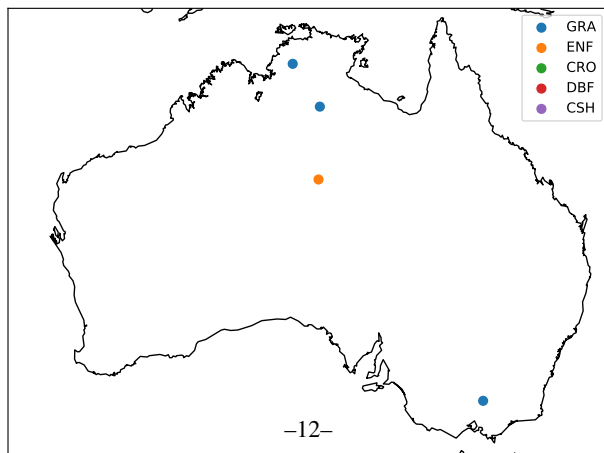
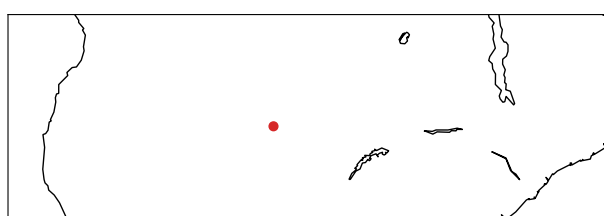
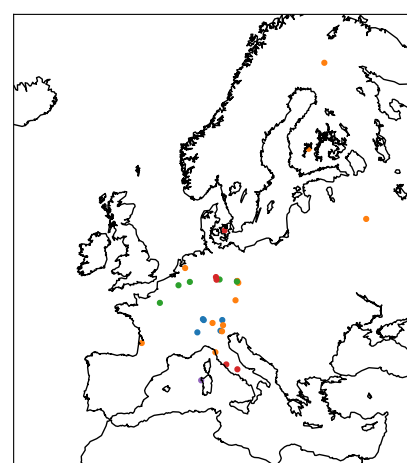
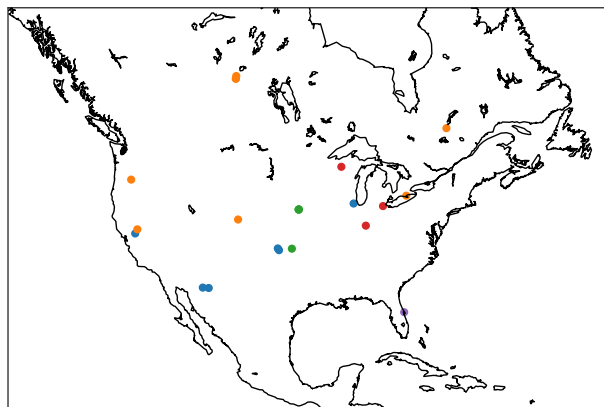
Franks, P. J., J. A. Berry, D. L. Lombardozzi, and G. B. Bonan (2017), Stomatal function across temporal and spatial scales: Deep-time trends, land-atmosphere coupling and

263 global models, *Plant Physiology*, 174(2), 583–602, doi:10.1104/pp.17.00287.

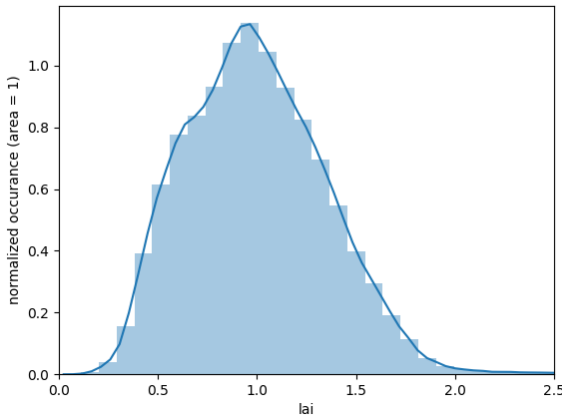
264 Lin, Y.-S., B. E. Medlyn, R. A. Duursma, I. C. Prentice, H. Wang, S. Baig, D. Eamus, V. R.
265 de Dios, P. Mitchell, D. S. Ellsworth, M. O. de Beeck, G. Wallin, J. Uddling, L. Tarvainen,
266 M.-L. Linderson, L. A. Cernusak, J. B. Nippert, T. W. Ocheltree, D. T. Tissue, N. K.
267 Martin-StPaul, A. Rogers, J. M. Warren, P. D. Angelis, K. Hikosaka, Q. Han, Y. Onoda,
268 T. E. Gimeno, C. V. M. Barton, J. Bennie, D. Bonal, A. Bosc, M. LÃºw, C. Macinins-
269 Ng, A. Rey, L. Rowland, S. A. Setterfield, S. Tausz-Posch, J. Zaragoza-Castells, M. S. J.
270 Broadmeadow, J. E. Drake, M. Freeman, O. Ghannoum, L. B. Hutley, J. W. Kelly,
271 K. Kikuzawa, P. Kolari, K. Koyama, J.-M. Limousin, P. Meir, A. C. L. da Costa, T. N.
272 Mikkelsen, N. Salinas, W. Sun, and L. Wingate (2015), Optimal stomatal behaviour
273 around the world, *Nature Climate Change*, 5(5), 459–464, doi:10.1038/nclimate2550.

274 MEDLYN, B. E., R. A. DUURSMA, D. EAMUS, D. S. ELLSWORTH, I. C. PRENTICE,
275 C. V. M. BARTON, K. Y. CROUS, P. D. ANGELIS, M. FREEMAN, and L. WINGATE
276 (2011), Reconciling the optimal and empirical approaches to modelling stomatal conduc-
277 tance, *Global Change Biology*, 17(6), 2134–2144, doi:10.1111/j.1365-2486.2010.02375.x.

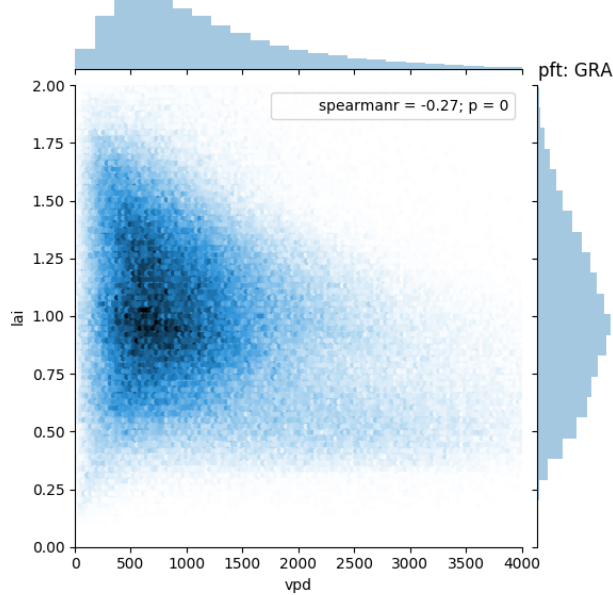
278 Zhou, S., B. Yu, Y. Huang, and G. Wang (2015), Daily underlying water use efficiency for
279 AmeriFlux sites, *Journal of Geophysical Research: Biogeosciences*, 120(5), 887–902, doi:
280 10.1002/2015jg002947.



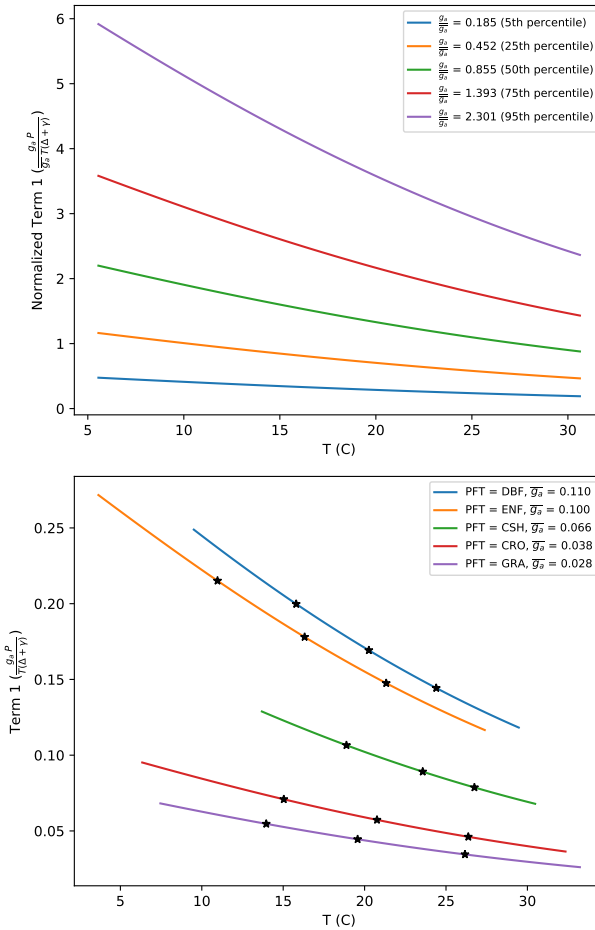
82 **Figure 1.** Plant functional type and location of sites used in analysis. ***This is just a placeholder for now
83 and needs to be improved i.e. with lat lon, better placement of continents, etc.)***



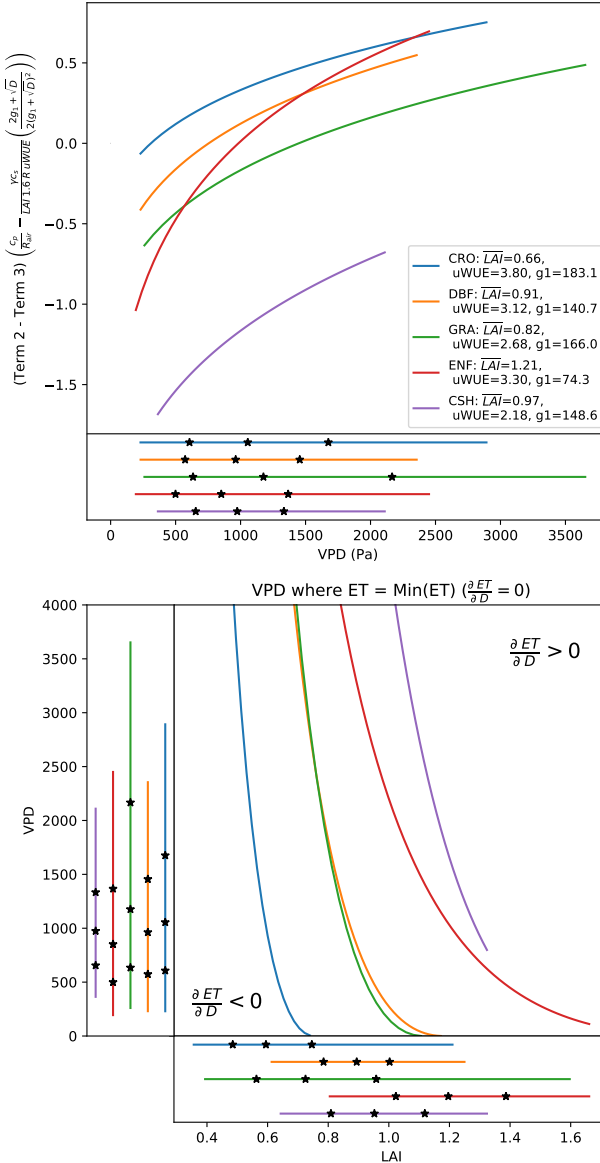
97 **Figure 2.** Histogram of LAI values calculated for each site and time according to Equation 8.
 98 The lowest and highest 5% are removed as outliers, as well as any values below 0. The curve is normalized such that its
 99 area is 1.



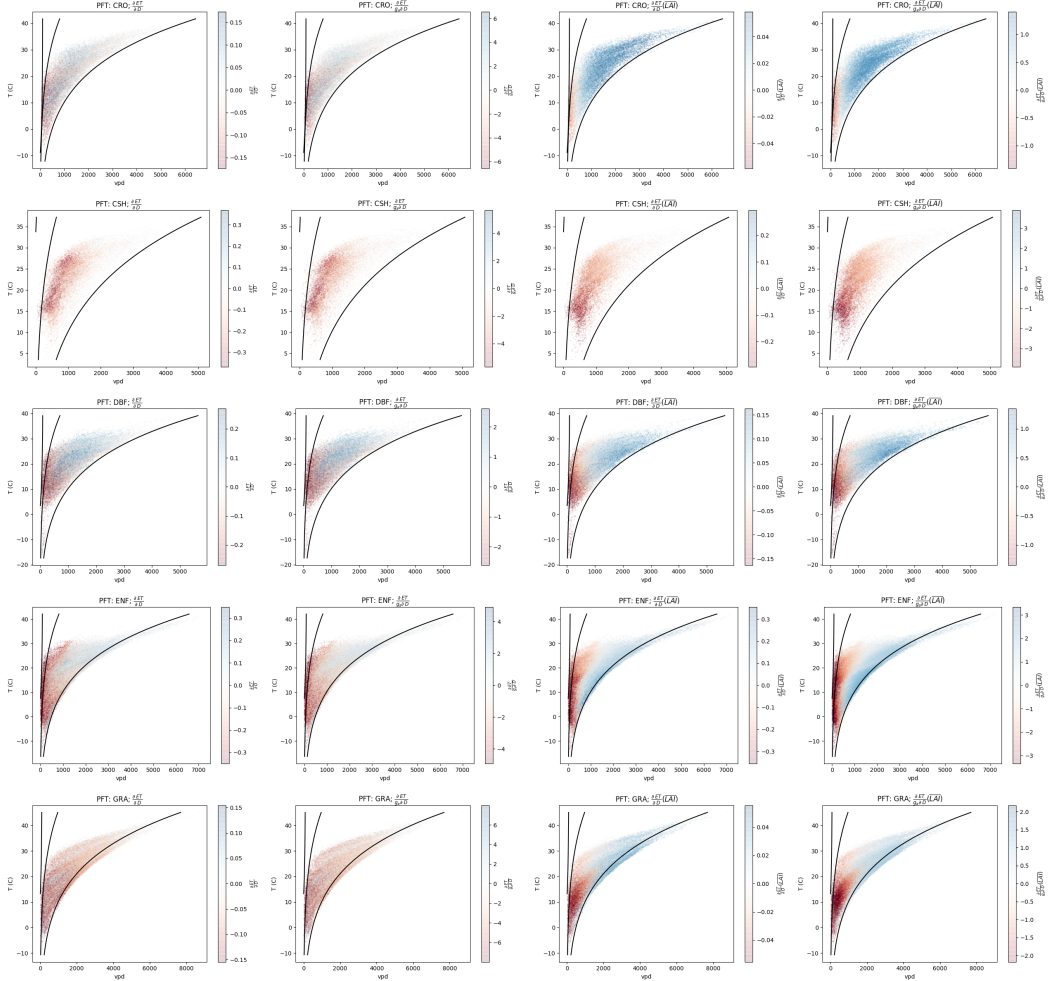
105 **Figure 3.** The joint distribution of D and LAI. LAI has only a weak dependence on D . ***This plot
 106 could probably benefit from a box plot of site specific correlations, because some sites do have stronger
 107 dependence than others. Note also Figs 3 and 2 can probably be combined because this figure shows LAI's
 108 histogram.***



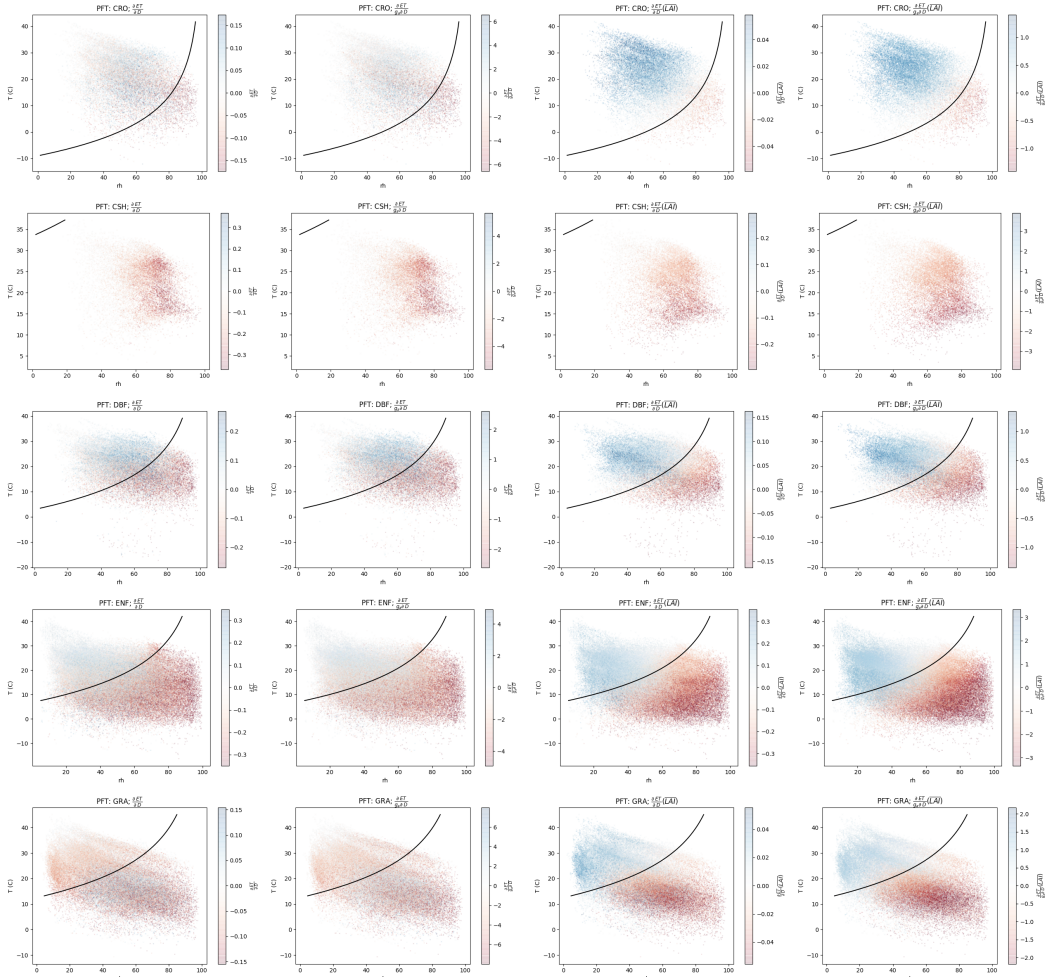
137 **Figure 4.** Primary sources of variability for Term 1. A) Variability within each PFT: Term 1 normalized by
 138 mean g_a for each PFT. B) Variability between each PFT: Term 1 evaluated at mean g_a for each PFT. Tempera-
 139 ture range is 5-95th percentile for each PFT. Additionally, stars denote the location of the 25th, 50th, and 75th
 140 percentiles.



148 **Figure 5.** Sources of variability for Term 2 - Term 3. Top: Term 2 - Term 3 as a function of VPD, with
 149 LAI held fixed at PFT averages. The observed range of VPD for each PFT is also shown below the x-axis.
 150 Line extent corresponds to 5th and 95th percentiles, while stars denote the location of the 25th, 50th, and 75th
 151 percentiles.
 152 Bottom: The location of the minima of ET, as a function of VPD and LAI. Lines and stars denote the distribu-
 153 tion of VPD and LAI next to each axis, following the same percentiles as above.



211 **Figure 6.** Scatter plots of $\frac{\partial ET}{\partial D}$. Each row is a different PFT, and each column is a different quantity related
 212 to $\frac{\partial ET}{\partial D}$, as labeled: Column 1 - $\frac{\partial ET}{\partial D}$; Column 2 - $\frac{\partial ET}{\partial D}$ normalized by g_a ; Column 3 - $\frac{\partial ET}{\partial D}$ with LAI held
 213 fixed at PFT average; and Column 4 - $\frac{\partial ET}{\partial D}$ normalized by g_a and with LAI held fixed. For reference, lines
 214 corresponding to RH = 20% and RH = 90 % are drawn. Please note differences in the colorbar scale. ***see
 215 alternate (or additional) plot below.***



223 **Figure 7.** ****alternate Fig 06**** Scatter plots of $\frac{\partial ET}{\partial D}$. Each column
 224 is a different quantity related to $\frac{\partial ET}{\partial D}$, as labeled. If I end up using this, I could also draw on the curve of
 225 $D_{ET\min}$ with \overline{LAI} .